Scientific Research Publishing

Journal of Transportation Technologies, 2026, 16(1), 77-94
https://www.scirp.org/journal/jtts
ISSN Online: 2160-0481
ISSN Print: 2160-0473

Finite Element Modeling and Validation of Submerged Arc Welding for Repairing 136RE Heavy Rails

Arman Ali Mohammadi[1], Zhiyong Wang[1], Hualiang Teng[2]

[1]Department of Mechanical Engineering, University of Nevada, Las Vegas, USA
[2]Department of Civil and Environmental Engineering and Construction, University of Nevada, Las Vegas, USA
Email: alimoham@unlv.nevada.edu, zhiyong.wang@unlv.edu, Hualiang.teng@unlv.edu

How to cite this paper: Mohammadi, A.A., Wang, Z.Y. and Teng, H.L. (2026) Finite Element Modeling and Validation of Submerged Arc Welding for Repairing 136RE Heavy Rails. *Journal of Transportation Technologies*, **16**, 77-94.
https://doi.org/10.4236/jtts.2026.161005

Received: October 14, 2025
Accepted: December 19, 2025
Published: December 22, 2025

Abstract

The constant wear and tear experienced by rail surfaces due to continuous loading necessitates repairs for maintaining optimal performance within railway networks. Traditional repair methods are not only time-consuming but also costly, motivating the exploration of innovative alternatives. This study focuses on the development of a finite element (FE) model to simulate the submerged arc welding (SAW) process, which serves as an additive manufacturing technique for restoring 136-lb/yd (136RE) rails, commonly utilized in heavy freight and passenger rail systems across the United States. To validate the developed FE model, a series of experimental laboratory investigations was conducted. A worn section of the 136RE rail was carefully chosen for this study. After the rail's surface underwent milling and flattening, the submerged arc welding process was employed to rebuild the rail, utilizing a 1/8-inch Lincore 40-S depositing wire. The reconstructed rail sample was then subjected to experimental tests, including tensile testing, which provided the essential mechanical properties required to validate the simulation process. The FE model encompasses all conceivable interactions, including thermal, mechanical, and phase transformations. This simulation employs an element-birth-and-kill method, examining the thermal distribution within the sample across different sections. By considering the thermal history and phase change relations, the model predicts the mechanical properties of the repaired rail. The validated model showcases substantial potential in exploring and predicting mechanical properties and thermal distribution during the SAW process for heavy rail repair.

Keywords

Submerged Arc Welding, Finite Element Analysis, Additive Manufacturing,

Rail Repair

1. Introduction

Rail tracks' durability is influenced by wear and rolling contact fatigue [1]. Various types of damage commonly arise on railway tracks, predominantly attributable to side wear, fatigue cracks, head checks, and spalling [2]. Switches, crossings, and curves are particularly prone to side wear, making their maintenance expenses significantly higher compared to straight sections of rail tracks. The primary cause of defects in rail tracks, mainly side wear, is the combination of normal and tangential stresses. Consequently, numerous studies have been undertaken to analyze and model the forces, moments, and contact area at the wheel/rail interface [3]-[7]. Rail defects have the potential to initiate and propagate cracks, ultimately causing spalling and, in severe cases, complete rail fracture. Consequently, another line of research has embraced rail grinding as a method to eliminate surface defects and prevent the progression of such cracks [8]-[10]. The grinding process can adversely affect rail longevity and increase operational costs [11] [12].

In response to the limitations of cost and weight in manufacturing rail profiles with high resistance to wear and rolling contact fatigue, the utilization of surface coatings as a form of surface treatment has gained prominence. Various surface coating technologies, such as shielded metal arc welding (SMAW), have been developed as alternative approaches based on specific applications and coating types. For instance, Saiful Akmal and Wahab researched the application of SMAW for repairing damaged surfaces of UIC-54 rails in the Malaysian railway network [13]. De Becker *et al.* [14] are also developing a mobile system for automated on-site repair of the railway network in the United Kingdom. Kabo *et al.* [15] developed a numerical model to examine the rolling contact fatigue performance and material defects in weld-repaired rails in Sweden. Furthermore, Xin *et al.* [16] conducted a valuable numerical study in the Netherlands, investigating repair welding and grinding of standard European rails using finite element modeling.

Regarding studying standard rails utilized in the United States railway system, the current research group is the sole entity concentrating on repairing them through overlay weld techniques. Previous investigations in the United States have explored laser cladding to repair damaged surfaces in both light transit rails [17] [18] and heavy freight/passenger rails [19]. Another research endeavor examined submerged arc welding (SAW) applications for repairing light rails [20]. This present study represents the first examination of the mechanical and metallurgical properties of a standard U.S. heavy rail undergoing SAW repair.

Repairing a damaged railhead surface offers significant advantages over conventional replacement methods, primarily due to its ease of implementation and avoiding extensive manipulation and reconstruction of the rail infrastructure. Although some minor surface grinding and cutting are necessary for overlay welding

on the railhead, this approach ensures that the original strength of the rail base is maintained. However, previous studies [21]-[25], including the author's research [17]-[20] have demonstrated that a surface-welded rail is more susceptible to cracking and premature failure than an integral parent rail. Consequently, conducting a comprehensive investigation into the strength properties, hardness, residual stress, and distribution of inclusions, pores, and cracks in a weld-repaired rail becomes essential. Notably, no study has been published that investigates explicitly the repair of heavy-duty rails used in the standard railway network of the United States using the submerged arc welding (SAW) method as mentioned in previous research [20], various arc-based methods, such as shielded metal arc welding (SMAW), gas tungsten arc welding (GTAW), submerged arc welding (SAW), and plasma arc welding (PAW), can be employed for surface welding. Among these methods, SAW is considered the most suitable for multi-layer, high-thickness welding due to its superior quality and productivity [26] [27].

In this research, a three-dimensional coupled temperature-displacement numerical model is developed using the commercial ANSYS software. This model aims to analyze the thermo-mechanical behavior of residual thermal stresses generated during the manufacturing of the worn part of the rail using the submerged arc welding (SAW) process. This specific configuration is referred to as Case I in the study. To examine the impact of preheating on thermal stresses, two additional cases involving different preheating methods and subsequent cooling rates are investigated to determine the optimal preheating approach. In Case II, preheating is applied by placing hot plates beneath the railhead during the cooling process of the additive part to reduce residual thermal stress. In Case III, hot plates are positioned at the railhead's bottom and sides. The results obtained from all three cases are compared to evaluate the state of thermal stress at the weld/rail interface. The safety margin of thermal stresses is determined by comparing the results to the yield strength of the material. The reported ~40% reduction refers to the relative decrease in interface residual stress compared to Case I.

2. Methodology

The current research follows a procedure based on the flowchart illustrated in **Figure 1**. First, a numerical method was defined based on the submerged arc welding method used to repair heavy rails, *i.e.*, 136RE rails. This model contains three steps that will be explained in the following sections: modeling only one pass of welding and finding welding parameters in this pass, modeling two dimensions of welding in a cross-section of rail and finding the temperature history of rail in welded section, and finding the structure of welded part based on temperature and Fe-Cr phase diagram. Finally, the result is verified based on the real sample.

The rail to be repaired in this study is a worn 136RE rail commonly employed in freight and passenger railway networks across the United States. The specimen analyzed in this research was a 30-cm section of the worn rail, as depicted in **Figure 2**. The chemical composition of the high-carbon steel utilized in manufactur-

ing the 136RE rail is provided in Table 1.

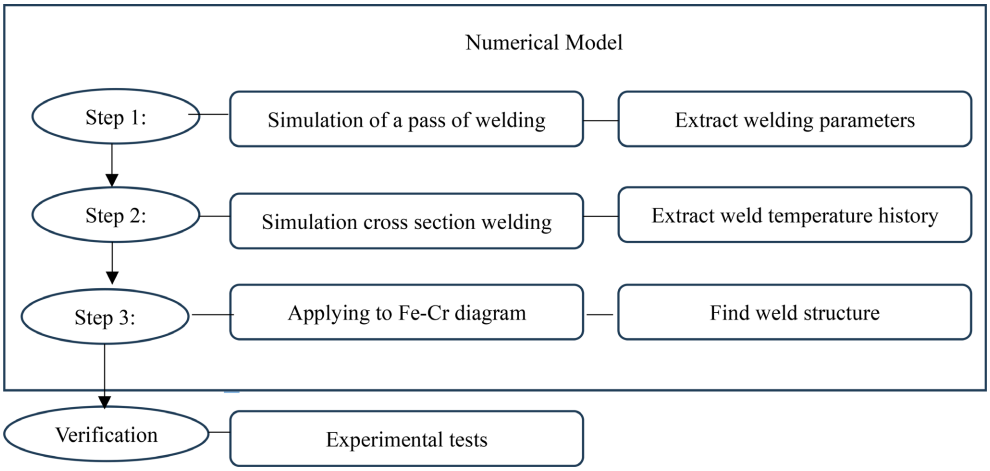

Figure 1. Methodology flowchart.

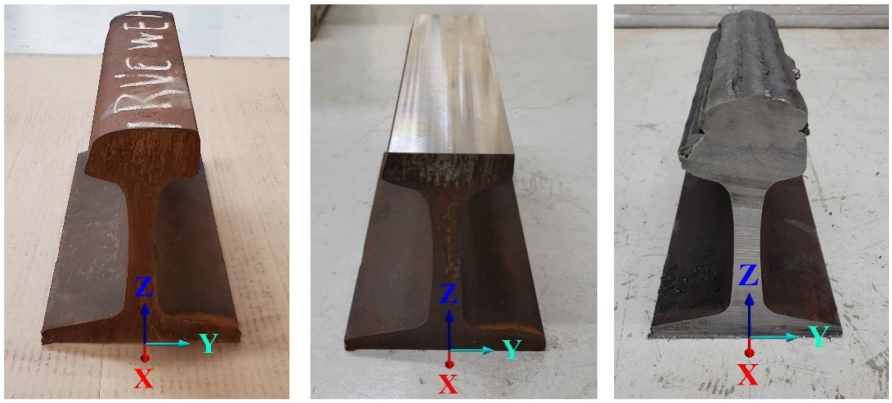

Figure 2. (a) The to-be-repaired 136RE worn rail; (b) Milled rail; (c) Repaired rail.

Table 1. Chemical composition of the rail and the SAW wire (wt.%).

Material	Fe	C	Cr	Mn	Mo	Si	Ni	P	S
Rail	Bal.	0.80 ± 0.06	0.03 ± 0.01	0.23 ± 0.03	-	0.04 ± 0.01	0.14 ± 0.04	0.01 ± 0.005	0.01 ± 0.005
Wire	Bal.	0.12 ± 0.05	0.50 ± 0.03	2.75 ± 0.30	0.85 ± 0.05	3.30 ± 0.20	-	-	-

For the SAW process, the selected depositing wire was the 1/8-inch Lincore 40-S hard-facing submerged arc wire. This specific wire was chosen due to its excellent characteristics in terms of rolling and sliding wear properties. Moreover, it is compatible with carbon steel and suitable for depositing up to 5 layers. The chemical composition of the SAW wire used is provided in Table 1. To complement the process, the neutral Lincolnweld 801 submerged arc flux was employed as the recommended and compatible flux, and its chemical composition is detailed in Table 2.

Table 2. Chemical composition of the neutral Lincolnweld 801 submerged arc flux (wt.%).

SiO_2	CO_2	CrO	MoO_3	MnO	Fe_2O_3
10.0 ± 0.9	21.2 ± 0.8	8.9 ± 0.2	18.4 ± 0.9	14.2 ± 0.8	22.7 ± 1.0

To facilitate the SAW process on a flat substrate, the surface of the worn railhead undergoes milling and flattening. Before commencing the SAW process, the milled surface is further prepared by grinding, polishing, and cleaning with acetone to eliminate loose mill scales, rust, and micro contaminants. The milled rail can be observed in **Figure 2(b)**, while **Figure 2(c)** depicts the rail after the SAW process, referred to as the surfaced rail. This emerged rail serves as the final product on which all mechanical and metallurgical assessments will be carried out.

The key distinction between conventional arc welding and SAW lies in covering flux. In SAW, the wire and the arc are effectively shielded beneath a layer of flux grains, protecting against oxidation. Another advantage of submerging the welding area within the flux stream is that it remains insulated from excessive radiation heat loss, resulting in a cleaner weld. By preventing potential heat loss mechanisms like radiation, convection, or energy scattering from wire to rail, the energy efficiency can be increased by 90% or even more. This heightened efficiency yields significant benefits, including enhanced weld reliability and a high deposition rate.

The SAW process involves the development of an arc between the filler wire and the railhead, which serves as the substrate. Simultaneously, flux grains are dispensed onto and around the arc area through a hopper. This forms a covering envelope at the arc zone, solidifying the melt pool on the railhead's surface where the arc is burned. The flux grains close to the envelope melt and solidify, forming a thin layer known as slag, which will be removed once the SAW process is completed. The current SAW process for overlay repairing the damaged railhead surface utilizes an open-circuit voltage ranging from approximately 25 to 36 V, a weld current of 150 A, a travel speed of 23 mm/s, and a wire feed rate of 21 mm/s.

3. Process Physical Description

In the following, Nomenclature and related Subscripts describe the process given. Also, the governing equations for this process are defined as follows:

- T temperature (K)
- x, y, z coordinate
- $\boldsymbol{V}$ velocity vector (m/s)
- u, v, w velocity component (m/s)
- $\boldsymbol{g}$ gravity vector (m^2/s)
- p pressure (Pa)
- ν kinematic viscosity (m^2/s)
- β thermal expansion coefficient (K^{-1})
- α_f thermal diffusivity of air (m^2/s)
- α_s thermal diffusivity of solid body (m^2/s)

- q_{in} incident radiative heat flux (W/m^2)
- q_{out} net radiative heat flux from the surface (W/m^2)
- Ω hemispherical solid angle (sr)
- I_{in} intensity of the incoming ray (W/sr)
- $\boldsymbol{s}$ ray direction vector
- $\boldsymbol{n}$ normal vector pointing out of the domain
- ε emissivity
- ϵ strain
- σ stress (Pa)
- C fourth-order material stiffness tensor (N/m)
- H' strain-hardening rate (Pa)
- ϑ Poisson's ratio
- E elastic modulus (Pa)
- e deviatoric strain
- γ engineering strain
- t time (s)

Subscripts

- h hot body
- c cold body
- w wall
- e elastic
- p plastic
- T thermal
- eq equivalent (von-Mises)
- zz longitudinal direction of principal stress
- xx transversal direction of principal stress
- yy normal direction of principal stress

Continuity equation:

$$\nabla \cdot \boldsymbol{V} = 0 \tag{1}$$

Momentum equation:

$$\frac{D\boldsymbol{V}}{Dt} = -\frac{1}{\rho}\nabla p + \nu\nabla^2\boldsymbol{V} + \boldsymbol{g}\beta\left(T - T_c\right) \tag{2}$$

Energy equation for fluid medium:

$$\frac{DT}{Dt} = \alpha_f\left(\nabla^2 \cdot T\right) \tag{3}$$

Energy equation for a still solid region without internal heat generation is: The volumetric heat input was derived from the welding current, voltage, arc efficiency, and travel speed, and then calibrated in the model to achieve the observed melt pool temperature (~1700˚C).

$$\frac{\partial T}{\partial t} = \alpha_s\left(\nabla^2 \cdot T\right) \tag{4}$$

The radiation intensity approaching a point on a wall surface can be integrated

to yield the incident radiative heat flux:

$$q_{in} = \int_{\boldsymbol{s}\cdot\boldsymbol{n}>0}^{q_{in}} I_{in}\boldsymbol{s}\cdot\boldsymbol{n}\mathrm{d}\Omega \tag{5}$$

The net radiative heat flux from the surface is then computed as:

$$q_{out} = \left(1-\varepsilon_w\right)q_{in} + \varepsilon_w \sigma T_w^4 \tag{6}$$

4. Numerical Modeling

To simulate the effects of thermal stresses, a three-dimensional model of the worn rail and weld layers is created using SolidWorks 2022. The new rail profile adheres precisely to the AREMA standard profiles (136 lb/yd [136RE]), while the worn profile is obtained from the provided rail specimen. The combined new and worn rail profiles are depicted in Figure 3.

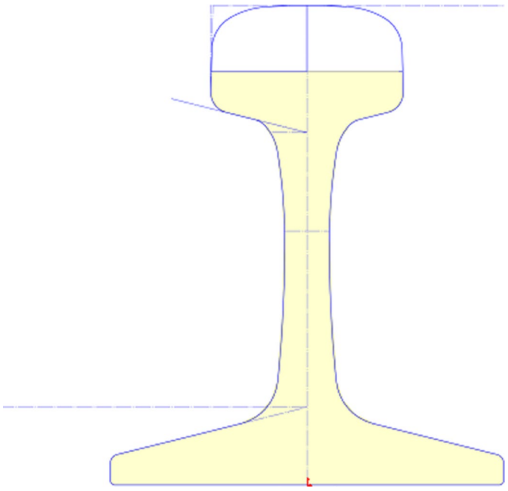

Figure 3. Original and worn rail profiles.

A grid independence test is performed during the thermal study (finite volume) step to reduce computational time and ensure confidence in the results. As a result, a grid system consisting of 90,792 elements is employed for calculations. Among these elements, 9792 belong to the rail part, and 81,000 are associated with the weld part. Different mesh zones generated in the solid bodies are illustrated in Figure 4. Three mesh densities were evaluated, and the selected mesh (90,792 elements) ensured convergence with less than approximately 3% variation in peak temperature and residual stress.

The model is divided into two sections: simulation of the process in a welding pass and simulation of the process in the entire cross-section area. This division is due to the nature of the welding process. After a complete row of welding, it can be assumed the entire row has the same temperature, and it should save a huge amount of calculation without losing much accuracy, considering that the first line of welding will also be simulated. Assuming that the additive layer in the 3D printing process reaches the temperature of 1700˚C and the ambient temperature (typical for SAW temperature) is 22˚C, the model is divided into two sets of ele-

ments with different material properties: the rail material and the weld material. The material properties are imported based on the data provided in Table 2.

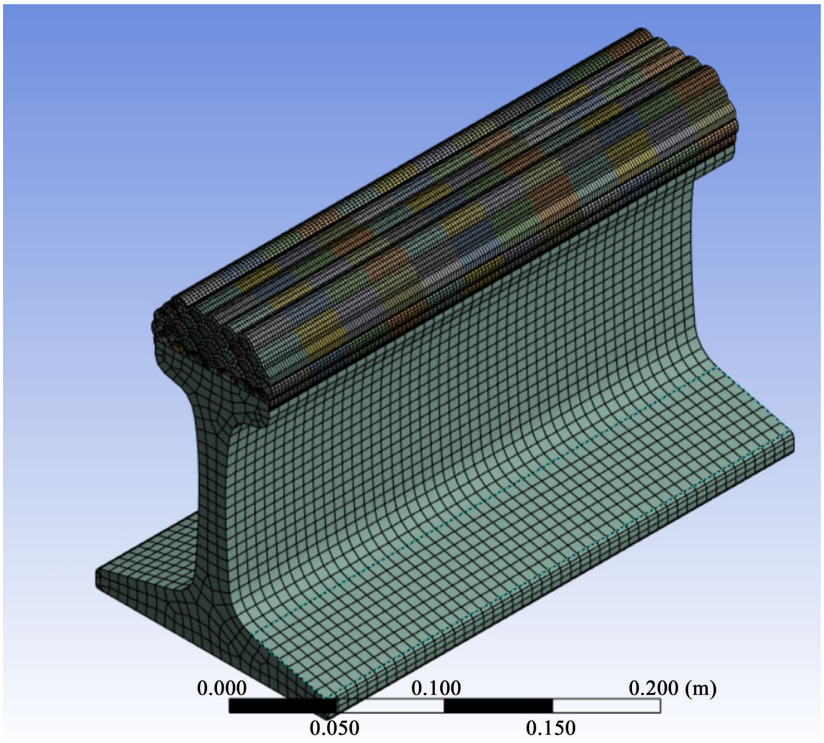

Figure 4. Mesh zones generated in the solid bodies.

The element birth-and-kill technique is incorporated to build up the worn part of the railhead in the FE. Each element was considered with a length of 25 mm, so there are 12 elements in each pass. According to welding speed, the time steps of this method are applied to the model. Considering this method, the welding process can be simulated as an internal heat generation with 3.8e009 W/m^3. The generated heat can be extracted from the current and voltage of the process by an adjustment to ensure that the melting pool's temperature will be provided (T = 1700˚C). The shape of the elements was estimated according to the actual weld profile in the real sample.

The thermal history field and subsequent residual stresses are analyzed through sequential thermo-mechanical analyses utilizing the commercial finite element code ANSYS 2023 R1. The thermal heat transfer analysis replicates the cooling process using the transient thermal method, and the results of this analysis are used as initial conditions for the subsequent finite element analysis.

5. Model Results

Using numerical modeling, comprehensive information can be obtained regarding temperature distribution. As before mentioned, to reduce the computational calculation, this model is divided into two main sections. In the first section, the model properties are validated by examining one welding row. In this regard, the

result is shown in Figure 5. Figure 6 also shows the procedure modeling. This model is a result of finite element try and error to find the optimum element size and heat generation properties as the controllable inputs.

The welding process is modeled on a 2D scale in the second step. In this section, only the first element got involved in the model. The first step's result shows that this assumption does not affect the entire process. Figure 7 illustrates the profile temperature result and historical temperature profile in the sample. This thermal history shows that in the Fe-Cr phase (Figure 8) what is the mechanical properties of the simulated maple. The dotted line in this diagram is according to Table 3.

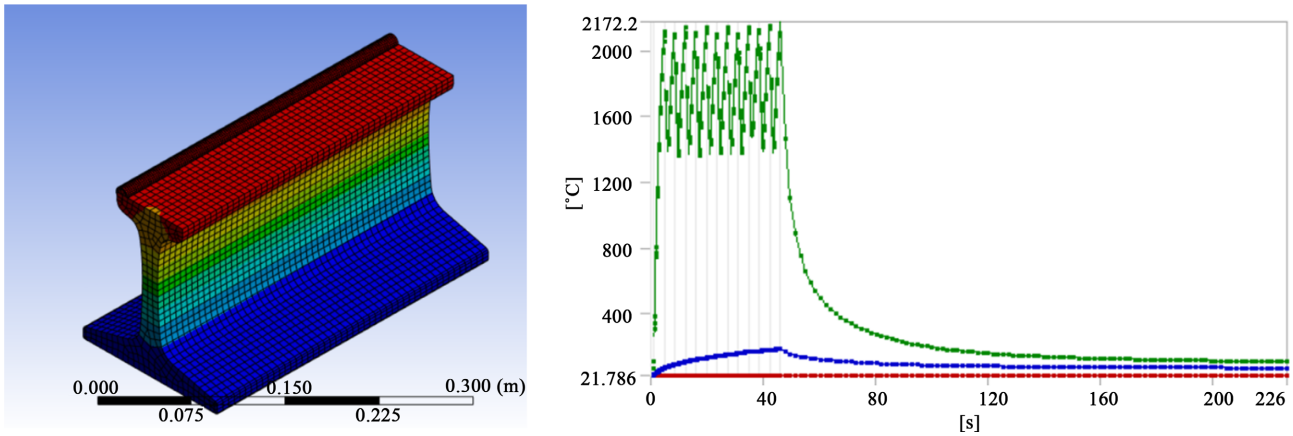

Figure 5. Graphical and numerical temperature distribution resulted from the model.

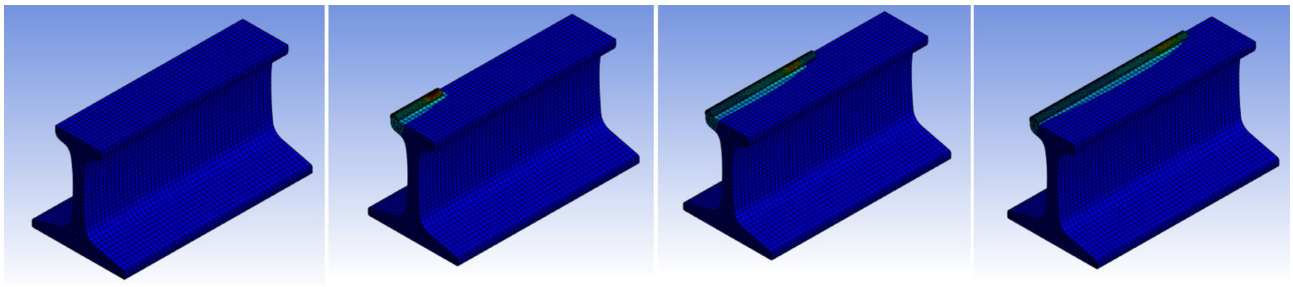

Figure 6. Graphical show of the model's procedure (step 1).

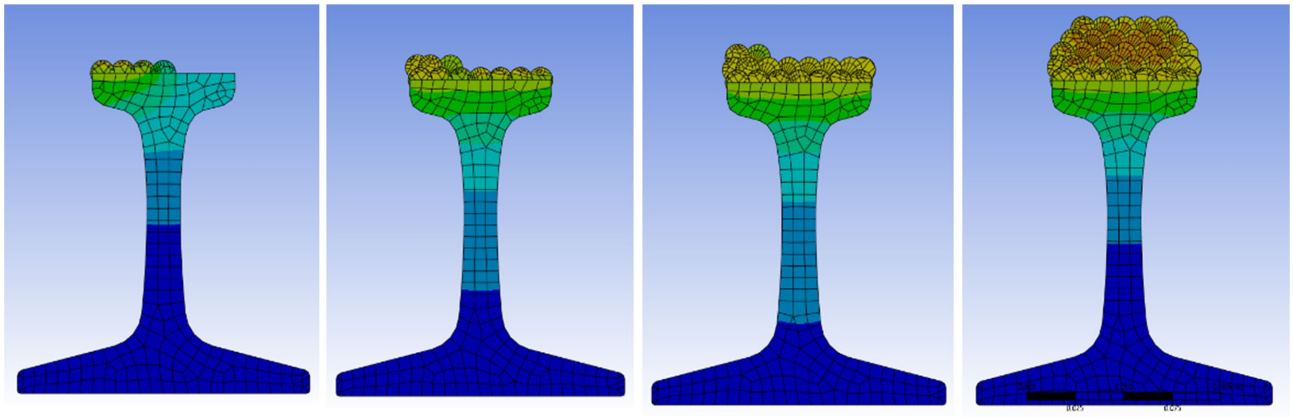

Figure 7. Graphical show of the model's procedure (step 2).

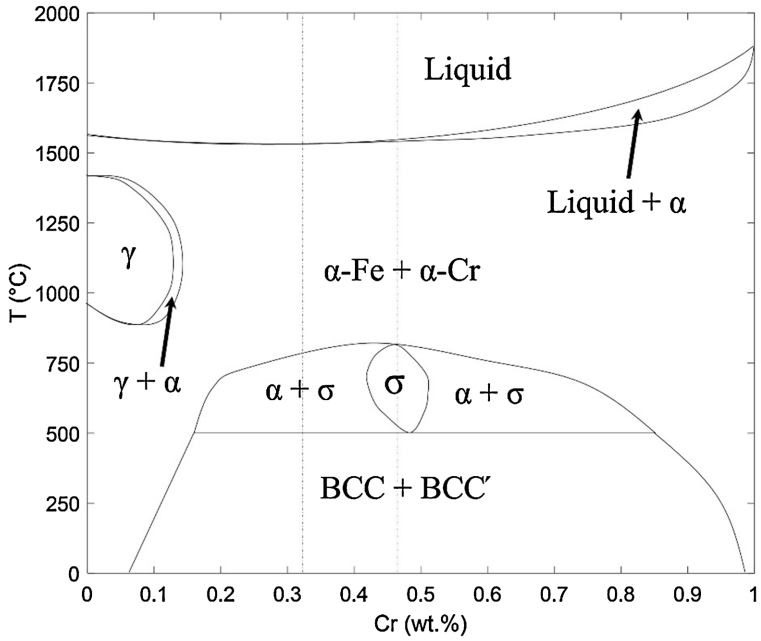

Figure 8. Fe-Cr phase diagram for the Lincore 40-S hard-facing wire used in the SAW process.

Table 3. Chemical composition (wt.%) of different areas of the repaired rail (Areas are addressed graphically in **Figure 4**).

Area	Fe	C	Cr	Mn	Mo	Si
Layer 4	Bal.	0.067 ± 0.007	0.32 ± 0.05	1.25 ± 0.20	0.82 ± 0.03	3.42 ± 0.40
Layer 3	Bal.	0.028 ± 0.007	0.39 ± 0.05	1.93 ± 0.20	0.80 ± 0.03	3.26 ± 0.40
Layer 2	Bal.	0.016 ± 0.007	0.41 ± 0.05	2.55 ± 0.20	0.73 ± 0.03	3.12 ± 0.40
Layer 1	Bal.	0.017 ± 0.007	0.47 ± 0.05	2.19 ± 0.20	0.73 ± 0.03	2.94 ± 0.40
HAZ	Bal.	0.23 ± 0.06	0.12 ± 0.01	1.01 ± 0.20	0.03 ± 0.01	0.53 ± 0.40
Rail	Bal.	0.80 ± 0.06	0.03 ± 0.01	0.23 ± 0.03	-	0.04 ± 0.01

The Fe-Cr phase diagram shows that the Lincore 40-S weld wire, containing approximately 0.5 wt.% chromium (as stated in **Table 1**), consists of a mixture of BCC phases with Fe-rich (BCC) and Cr-rich (BCC') alloy compounds at room temperature. At $0 \leq$ Cr-wt.% < 0.12, the austenite with the lightest appearance in HCl-etched carbon steel nucleates. Then, at Cr-wt.% ≥ 0.12, a combined α-Fe + α-Cr phase forms, which starts with the dominancy of the light-etched α-Fe at Cr-wt.% = 12 and smoothly transforms to a dark-etched, α-Cr-dominant compound as the Cr-wt.% leans towards 1.

Table 3 shows a declined flow of Cr-wt.% from Layer 1 to Layer 4. The liquidus weld drops at 1600˚C - 1700˚C, and the preheated railhead surface has a temperature of 200˚C - 300˚C, so the weld materials start to experience an initially fast cooling procedure down to 500˚C - 700˚C during the first layer. At the beginning of the second layer, Layer 1 is reheated and has a long exposure at a higher tem-

perature range, 700˚C - 1000˚C. Layer 2, with a higher initial substrate temperature (500˚C - 700˚C), remains at elevated temperatures around 700˚C - 1000˚C until the third layer starts. This trend proves that the top layers are exposed to higher temperature ranges, *i.e.*, higher than 500˚C - 800˚C. Prolonged exposures to temperatures in the range of 500˚C - 800˚C give enough time for the $\alpha \rightarrow \sigma$ transition—besides, a higher wt.% of Cr results in higher precipitated σ but lower Cr-wt.% gives a lower fraction of the brittle σ phase in the final microstructure. This explains why the semi-dark σ fraction decreases from Layer 1 to 4. By moving to the upper layers, the number of reheating opportunities (and the length of the 500˚C - 800˚C exposure time) decreases, hence the chance of $\alpha \rightarrow \sigma$ decreases. Another observable fact is that, as the Cr-wt.% decreases from Layer 1 to Layer 4 (Table 3), the volume fraction of the Cr-rich α, *i.e.*, α-Cr, falls, and that of the Fe-rich α, *i.e.*, α-Fe, increases. Therefore, Layer 1 contains the highest, and Layer 4 has the lowest amount of this dark α-Cr volume fraction among layers. In addition, the wt.% of the ferrite stabilizers (Mo and Si) has an increasing trend from Layer 1 to Layer 4 (Table 3), leading to the increment of the ferrite phase and increasing the light-etched α-Fe area in the upper layers.

This diagram shown in Figure 8 is modeled in the computational model based on the following diagrams. These diagrams are the linear forms of the phase diagram. The results are shown in Figure 9, with Table 4 as the numerical basis.

Table 4. Temperature- and Microstructure-Dependent Material Properties of Substrate (Rail) and Deposition Materials; Used in Fe Modeling of Additive Manufacturing (LPD) Process.

Material		T (˚C)	E (GPa)	ν	α (10^{-5}/˚C)	c (J/kg˚C)	K (W/m˚C)
304L Stainless Steel (Deposition Material)	δ	25	-	-	-	-	-
		600	134	0.34	1.73	745	18.9
		1000	19	0.41	1.82	984	15.5
		1500	19	0.41	1.82	971	13.2
	γ	25	200	0.29	1.73	510	15.5
		600	141	0.37	1.87	687	22.4
		1000	19	0.45	1.97	953	28.7
		1500	-	-	-	-	-
C-Mn (880 grade) steel (Substrate Material)	$\alpha + Fe_3C$	25	203	0.26	1.20	434	60.50
		600	110	0.33	1.40	638	41.60
		1000	-	-	-	-	-
		1500	-	-	-	-	-
	γ	25	-	-	-	-	-
		600	-	-	-	-	-
		1000	19	0.40	1.47	886	12.60
		1500	19	0.40	1.47	886	12.60

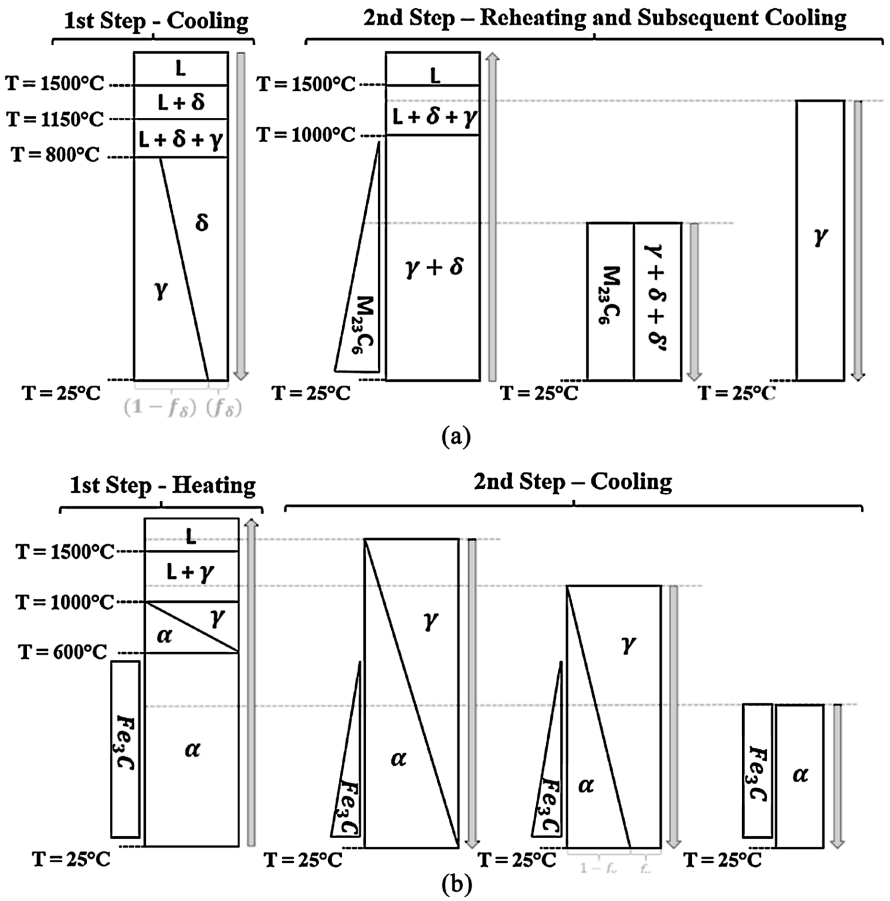

Figure 9. A schematic diagram of the microstructure evolution pattern defined in fe modeling during the additive manufacturing (LPD) process, and its cyclic heating and cooling for (a) deposition materials (304l stainless steel), and (b) substrate (rail). δ: δ Ferrite; *α*: *α* Ferrite; and γ: Austenite.

Consistent with prior studies [18]-[20], 304 L stainless steel was used as a proxy for Lincore 40-S due to similar Fe-Cr ferritic-austenitic phase transformation behavior at elevated temperatures.

6. Experimental Validation

6.1. Hardness Test

The Rockwell C hardness test is the best scale for high/mild carbon steels, conforming to ASTM E18 [28]. The Rockwell C scale's applied major and minor loads are 150 kgf and 10 kgf, respectively. A LECO hardness tester is used for this purpose. **Figure 10(e)** shows the assigned test plan on the transverse section, using the slices cut from the repaired rail shown in **Figure 10(b)** based on the test protocol provided by the American Railway Engineering and Maintenance-of-way Association (AREMA) [29].

6.2. Tensile Test

The prepared tensile samples are illustrated in **Figure 10(f)** and **Figure 10(i)**. Four

specimens are extracted from different regions of the base railhead and weld. The test method follows ASTM E8M, and the load requirement is assigned as per AREMA [29]. The test specimens are machined and dimensioned based on ASTM E8M. The standard test jig, recommended by ASTM E8M, is bundled with a hydraulic compression system as the major component of the test setup. A constant crosshead velocity of 2.5 mm/min is used for the tensile test.

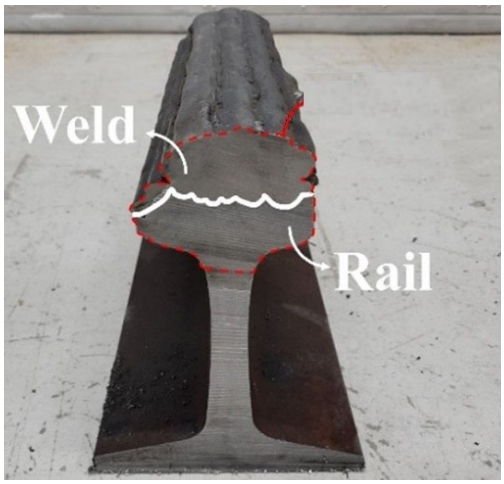

(a)

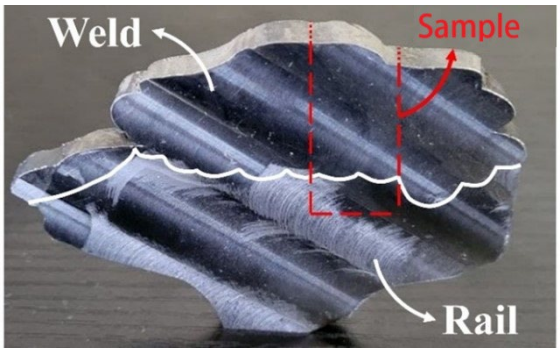

(b)

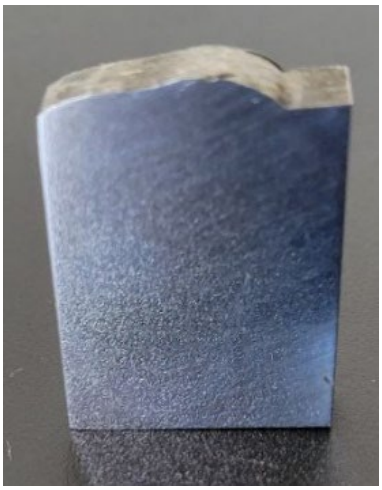

(c)

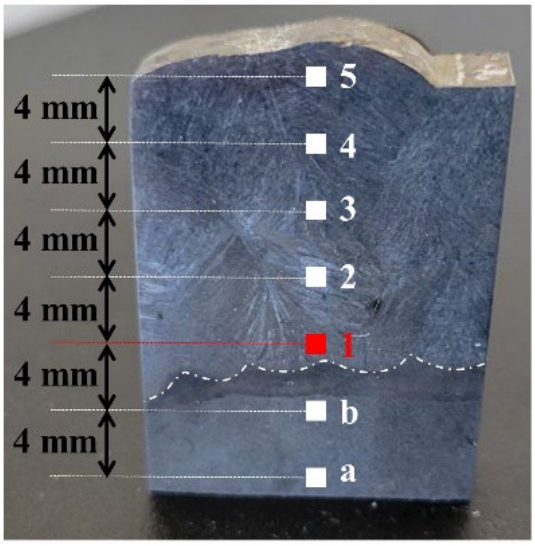
4 mm
4 mm
4 mm
4 mm
4 mm
4 mm
5
4
3
2
1
b
a

(d)

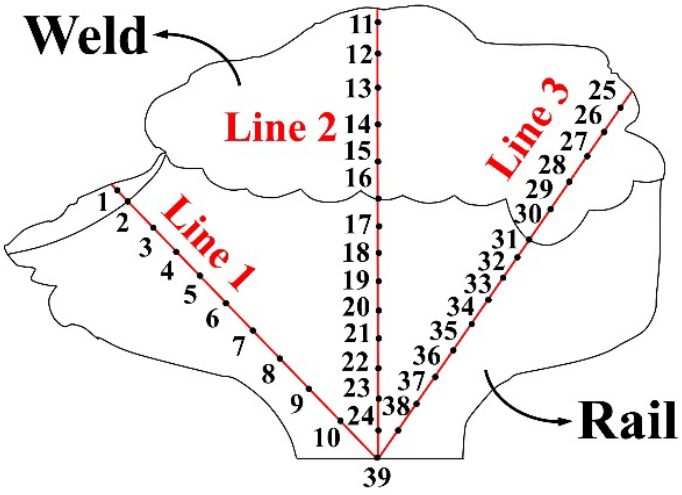
Weld
Line 1
Line 2
Line 3
Rail
1
2
3
4
5
6
7
8
9
10
11
12
13
14
15
16
17
18
19
20
21
22
23
24
25
26
27
28
29
30
31
32
33
34
35
36
37
38
39

(e)


75
13

(f)

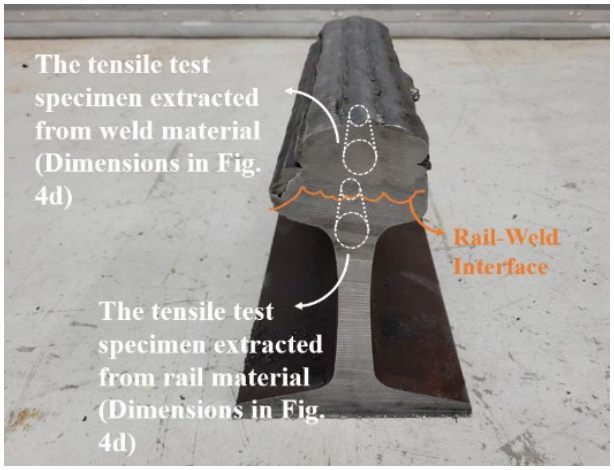

(g)

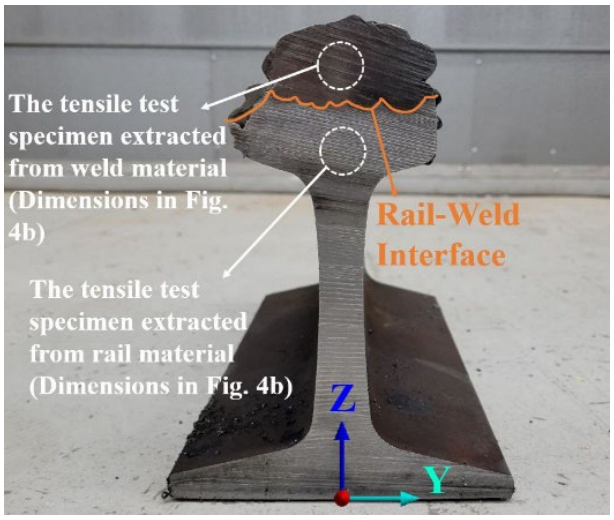

(h)

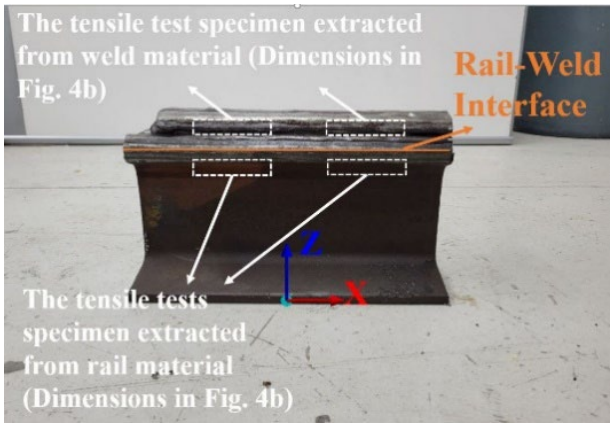

(i)

Figure 10. (a) The Repaired Rail; (b) The extracted slice from the repaired rail; (c) The extracted, polished XRD specimen from the slice; (d) The etched XRD specimen; (e) The hardness test plan; (f) Dimensions of a typical tensile test specimen (all dimensions are in millimeters); (g)-(i) Locations where the tensile specimens are extracted from the weld and the rail materials.

7. Conclusions

In this study, a 3D model was created and a coupled finite volume-finite element method was utilized to investigate the thermo-mechanical effects of high-temperature additive materials on the rail during the SAW process for repair purposes on worn rails. Three cases were examined to analyze the impact of preheating on the residual thermal stress induced at the rail/additive interface. The key findings can be summarized as follows:

1) In phase one, the stress distribution revealed that in each pass of welding, the temperature result leans to a temperature, which in the second phase is used in the rest of the conclusion.

2) To mitigate the rapid cooling rate, Case II was introduced, where two hot plates were placed at the bottom of the railhead to maintain elevated temperatures at the rail and rail/additive interface for a longer duration. This approach led to a reduction of approximately 40% in the final induced thermal stress. However, both Case I and Case II exhibited a sudden increase in stress at the edges of the transversal line of the rail/weld interface. This phenomenon occurred because the edge points experienced the fastest cooling rate due to direct exposure to airflow and the ambient wall. Consequently, these points rapidly lost heat through various heat transfer mechanisms, including conduction, convection, and radiation.

3) To address this issue, Case III was introduced, where two additional hot plates were positioned at the sides of the railhead. By doing so, these hot plates shielded the edges of the interface from direct exposure to the ambient environment. It was observed that this approach effectively mitigated the residual stresses at the edges, eliminating the sudden stress increases observed in the previous cases.

Overall, the study demonstrated the influence of numerical methods in simulation of welding process on the distribution of residual thermal stress at the rail/weld interface. The findings highlighted the importance of controlling the cooling rate and providing thermal insulation to minimize thermal stresses and ensure the integrity of the printed components.

Conflicts of Interest

The authors declare no conflicts of interest regarding the publication of this paper.

References

[1] Lewis, S.R., Lewis, R. and Fletcher, D.I. (2015) Assessment of Laser Cladding as an Option for Repairing/Enhancing Rails. *Wear*, **330**, 581-591. https://doi.org/10.1016/j.wear.2015.02.027

[2] Wang, W.J., Hu, J., Guo, J., Liu, Q.Y. and Zhu, M.H. (2014) Effect of Laser Cladding on Wear and Damage Behaviors of Heavy-Haul Wheel/Rail Materials. *Wear*, **311**, 130-136. https://doi.org/10.1016/j.wear.2014.01.011

[3] Paul, B. (1975) A Review of Rail-Wheel Contact Stress Problems. Report No. FRA OR&D 76-141.

[4] Montenegro, P.A. and Calçada, R. (2023) Wheel-Rail Contact Model for Railway Vehicle-Structure Interaction Applications: Development and Validation. *Railway Engineering Science*, **31**, 181-206. https://doi.org/10.1007/s40534-023-00306-4

[5] Liu, B. and Bruni, S. (2015) Analysis of Wheel-Roller Contact and Comparison with the Wheel-Rail Case. *Urban Rail Transit*, **1**, 215-226. https://doi.org/10.1007/s40864-015-0028-3

[6] Telliskivi, T. and Olofsson, U. (2001) Contact Mechanics Analysis of Measured Wheel-Rail Profiles Using the Finite Element Method. *Proceedings of the Institution of Mechanical Engineers, Part F: Journal of Rail and Rapid Transit*, **215**, 65-72. https://doi.org/10.1243/0954409011531404

[7] Yan, W. and Fischer, F.D. (2000) Applicability of the Hertz Contact Theory to Rail-Wheel Contact Problems. *Archive of Applied Mechanics (Ingenieur Archiv)*, **70**, 255-268. https://doi.org/10.1007/s004199900035

[8] Zhai, W., Gao, J., Liu, P. and Wang, K. (2014) Reducing Rail Side Wear on Heavy-Haul Railway Curves Based on Wheel-Rail Dynamic Interaction. *Vehicle System Dynamics*, **52**, 440-454. https://doi.org/10.1080/00423114.2014.906633

[9] Zarembski, A.M. (2005) The Art and Science of Rail Grinding. Simmons-Boardman Books.

[10] Kapoor, A., Beynon, J.H., Fletcher, D.I. and Loo-Morrey, M. (2004) Computer Simulation of Strain Accumulation and Hardening for Pearlitic Rail Steel Undergoing Repeated Contact. *The Journal of Strain Analysis for Engineering Design*, **39**, 383-396. https://doi.org/10.1243/0309324041223935

[11] Tunna, J., Sinclair, J. and Perez, J. (2007) A Review of Wheel Wear and Rolling Contact Fatigue. *Proceedings of the Institution of Mechanical Engineers, Part F: Journal of Rail and Rapid Transit*, **221**, 271-289. https://doi.org/10.1243/0954409jrrt72

[12] Mazzù, A., Petrogalli, C. and Faccoli, M. (2015) An Integrated Model for Competitive Damage Mechanisms Assessment in Railway Wheel Steels. *Wear*, **322**, 181-191. https://doi.org/10.1016/j.wear.2014.11.013

[13] SaifulAkmal, M.N. and Wahab, M.N. (2021) Characterization of UIC-54 Rail Head Surface Welded by Hard Facing Using Flux-Cored Steel Wire. In: Osman Zahid, M.N., Abdul Sani, A.S., Mohamad Yasin, M.R., Ismail, Z., Che Lah, N.A. and Mohd Turan, F. Eds., *Lecture Notes in Mechanical Engineering*, Springer, 763-775. https://doi.org/10.1007/978-981-15-9505-9_68

[14] De Becker, D., Dobrzanski, J., Goh, M. and Justham, L. (2020) Towards the Development of a Deposition Technology for an Automated Rail Repair System. *UK-RAS Conference for PhD and Early Career Researchers Proceedings*, 17 April 2020, 100-102. https://doi.org/10.31256/vz2jt4i

[15] Kabo, E., Ekberg, A. and Maglio, M. (2019) Rolling Contact Fatigue Assessment of Repair Rail Welds. *Wear*, **436**, Article 203030. https://doi.org/10.1016/j.wear.2019.203030

[16] Xin, L., Markine, V. and Shevtsov, I. (2018) Analysis of the Effect of Repair Welding/Grinding on the Performance of Railway Crossings Using Field Measurements and Finite Element Modeling. *Proceedings of the Institution of Mechanical Engineers, Part F: Journal of Rail and Rapid Transit*, **232**, 798-815. https://doi.org/10.1177/0954409717693960

[17] Mortazavian, E., Wang, Z. and Teng, H. (2022) Effect of Heat Treatment on Microstructure and Hardness of a Worn Rail Repaired Using Laser Powder Deposition. *International Journal of Transportation Science and Technology*, **11**, 406-422. https://doi.org/10.1016/j.ijtst.2021.05.004

[18] Mortazavian, E., Wang, Z. and Teng, H. (2021) Finite Element Investigation of Thermal-Kinetic-Mechanical Evolutions during Laser Powder Deposition as an Innovative Technique for Rail Repair. *The International Journal of Advanced Manufacturing Technology*, **118**, 319-342. https://doi.org/10.1007/s00170-021-07873-y

[19] Mortazavian, E., Wang, Z. and Teng, H. (2021) Measurement of Residual Stresses in Laser 3D Printed Train Rail Using X-Ray Diffraction Technique. *ASME International Mechanical Engineering Congress and Exposition*, online. 1-5 November 2021, 9. https://doi.org/10.1115/IMECE2021-69822

[20] Mortazavian, E., Wang, Z. and Teng, H. (2020) Repair of Light Rail Track through Restoration of the Worn Part of the Railhead Using Submerged Arc Welding Process. *The International Journal of Advanced Manufacturing Technology*, **107**, 3315-3332. https://doi.org/10.1007/s00170-020-05208-x

[21] Josefson, B.L. and Ringsberg, J.W. (2009) Assessment of Uncertainties in Life Prediction of Fatigue Crack Initiation and Propagation in Welded Rails. *International Journal of Fatigue*, **31**, 1413-1421. https://doi.org/10.1016/j.ijfatigue.2009.03.024

[22] Masoudi, A., Davarpanah Jazi, M., Mohrekesh, M. and Masoudi Nejad, R. (2022) An Investigation of Rail Failure Due to Wear Using Statistical Pattern Recognition Techniques. *Engineering Failure Analysis*, **134**, Article 106084. https://doi.org/10.1016/j.engfailanal.2022.106084

[23] Desimone, H. and Beretta, S. (2006) Mechanisms of Mixed Mode Fatigue Crack Propagation at Rail Butt-Welds. *International Journal of Fatigue*, **28**, 635-642. https://doi.org/10.1016/j.ijfatigue.2005.07.044

[24] Skyttebol, A., Josefson, B.L. and Ringsberg, J.W. (2005) Fatigue Crack Growth in a Welded Rail under the Influence of Residual Stresses. *Engineering Fracture Mechanics*, **72**, 271-285. https://doi.org/10.1016/j.engfracmech.2004.04.009

[25] Masoudi Nejad, R., Liu, Z., Ma, W. and Berto, F. (2021) Fatigue Reliability Assessment of a Pearlitic Grade 900A Rail Steel Subjected to Multiple Cracks. *Engineering Failure Analysis*, **128**, Article 105625. https://doi.org/10.1016/j.engfailanal.2021.105625

[26] Team Xometry (2023) Submerged Arc Welding (SAW): Definition, Purpose, and How It Works. https://www.xometry.com/resources/sheet/submerged-arc-welding-saw/

[27] Moshi, A.M.A., Sundara Bharathi, S.R., Rajeshkumar, R. and Kumar, R. (2016) Factors Influencing Submerged Arc Welding on Stainless Steel—A Review. *ARPN Journal of Engineering and Applied Sciences*, **11**, 1237-1241.

[28] (2025) ASTM E18: Hardness Testing of Metals and Alloys. https://www.samaterials.com/blog/astm-e18-hardness-testing-of-metals-and-alloys.html

[29] American Railway Engineering and Maintenance-of-Way Association (2014) Manual for Railway Engineering.